Comparison of structural and optical properties of CeO_2 and CeO_2:Eu^{3+} nanoparticles synthesized via sol–gel and flame spray pyrolysis methods

Serdar Yildirim[1,2,3] · S. Alper Akalin[1,3] · Sibel Oguzlar[1] · Merve Zeyrek Ongun[4] · Caglar Ozer[3] · Mustafa Erol[2,3]

Abstract

Over the last decades, a considerable attention has been drawn on the cerium dioxide (ceria, CeO_2) due to promising changes in physical and chemical properties in nanoscale. The researches on CeO_2 and its structural and morphological modifications have brought about remarkable applications as optical devices, sensors, medical equipments and luminescent materials. For instance, rare earth (RE) ion-doped cerium oxides have exhibited enhanced peculiar optical, catalytic and magnetic properties with respect to the dopant-free CeO_2 nanoparticles. Herein we aimed to compare characteristics of undoped (CeO_2) and europium (Eu^{3+}) doped ceria (CeO_2:Eu^{3+}) nanoparticles synthesized by sol–gel (SG) and one-step flame spray pyrolysis (FSP) methods. In this work, fabricated nanoparticles were evaluated in terms of the structural, morphological, chemical and optical properties by using X-ray diffraction (XRD), scanning electron microscopy (SEM), X-ray photoelectron (XPS) and photoluminescence spectroscopy (PL), respectively. Nanoparticles in the intended crystalline CeO_2 structure were obtained for both methods. Spherical particles in nanoscale (particle size < 100 nm) and sharp edged blocky particles in sub-micron size (particles size range 200–1000 nm) were produced through FSP and SG, respectively. Nevertheless, no significant difference due to the difference in particle size was observed in optical properties. On the other hand, Eu^{3+} doped particles of both methods exhibited longer decay time than the undoped particles.

1 Introduction

Recently, there has been considerable interest in preparation, characterization and applications of metal oxide nanoparticles that play a key role in several technologies. The metal oxide nanoparticles that used in the piezoelectric, optoelectronic and sensor applications show excellent chemical and physical specifications because of having limited size and high edge surface sites. There are many types of metal oxide nanoparticles as MgO, Al_2O_3, CeO_2, ZrO_2, AgO, NiO and TiO_2 oxide. Al_2O_3 material has importance as a catalyst component; MgO has wide application for as a scrubber for air pollutant gases; ZrO_2 has application as a solid electrolyte, gas sensor as well as a catalyst; TiO_2 is one of the most common oxide material used for various kinds of industrial applications about catalysis, photocatalysis, organic synthesis and etc. [1]. Among them, cerium dioxide (ceria, CeO_2) nanoparticles particularly plays a major role in a wide variety of technological applications as; catalysis, luminescence-based optical sensors, biology and medical applications thanks to distinct physical, chemical and optical properties [2, 3]. Today, pristine ceria and its metal incorporated modifications have also been attracted attention owing to their strong optical properties and the excitation of the activator ions by energy transfer. Moreover, incorporation of rare earth ions into cerium dioxide, led to act as luminescent activators due to the strong emission lines based on their sharp 4–4f intra-shell transitions [4].

As a rare earth, europium (Eu^{3+}) have been incorporated of into cerium dioxide structure by several groups. Li and co-workers reported that Eu^{3+} concentration in CeO_2 crystal

✉ Serdar Yildirim
serdar.yildirim@deu.edu.tr

1 Center for Fabrication and Application of Electronic Materials, Dokuz Eylul University, Buca, 35390 Izmir, Turkey

2 Department of Metallurgical and Materials Engineering, Dokuz Eylul University, Buca, 35390 Izmir, Turkey

3 Department of Nanoscience and Nanoengineering, Dokuz Eylul University, Buca, 35390 Izmir, Turkey

4 Izmir Vocational High School, Chemistry Technology Program, Dokuz Eylul University, Buca, 35390 Izmir, Turkey

lattice up to 1.0 wt% resulted in the observation of red shifts at the excitation spectrum. However, for the concentrations 5 and 10 wt% they recorded blue shifts. Eu^{3+} ions with the low concentrations (< 1.0 wt%) no distortion in the cubic fluorite structure of CeO_2 was observed while in higher concentrations (> 1.0 wt%), the sites of Eu^{3+} ions are strongly affected by the oxygen vacancies [5]. In another study, Vimal et al. declared the optimum doping concentration of Eu^{3+} as 1.5 wt% since an emission quenching was observed at 617 nm for the concentrations up to 2.0 wt% [6].

There are many different approaches applied for the production of both, CeO_2 and CeO_2:Eu^{3+} nanoparticles such as flame spray pyrolysis, sol–gel, micro-emulsion, hydrothermal, radio frequency magnetron sputtering solid-reaction, and electrodeposition [5, 7–13]. In the present study, Eu^{3+} doped and un-doped ceria nanocrystals were synthesized using both of the SG and the FSP methods. As stated in previous literatures [5, 6] the optimum Eu^{3+} ratio in CeO_2 was determined as 1.5 wt% for both methods. Many advantages including rapid growth, increased reaction rate and shortened reaction time, make the FSP technique as the mostly preferred method for synthesizing many nanocrystals. The capacity to disperse the precursor immediately in the fuel, the simplicity of the introduction of the precursor into the hot reaction area and the flexibility in using the high-velocity spray jet for rapid quenching of aerosol formation are the advantages of FSP [14]. Therefore the FSP technique has been used many times in the production of a wide variety of compositions as metal oxides, complex oxides, and nanocomposites used in a number of emerging applications such as photo-catalysis, sensors, batteries and solar cells [15, 16]. On the other hand, the SG process can be easily controlled in terms of the effect of a diversity of synthesis parameters as gelation time, the temperature of calcination and dwell time on chemical composition and crystallite size during the synthesis of nanoparticles.

In the literature, there is no other sample of work about the comparison of two methods for the synthesis of the CeO_2 and Eu^{3+}-doped CeO_2 nanoparticles to the best of our knowledge. With this motivation, in this work, we studied the structural characterization and optical properties of the nanoparticles synthesized by SG and FSP methods. The fabricated nanoparticles were characterized by using X-ray diffractometer (XRD), X-ray photoelectron spectroscopy (XPS), scanning electron microscopy (SEM) photoluminescence (PL) and decay time measurements.

2 Experimental studies

In order to produce nano-powders by both FSP and SG, cerium(III) acetylacetonate hydrate [Ce(C$_5$H$_7$O$_2$)$_3$·xH$_2$O, anhydrous basis] and europium(III) nitrate pentahydrate

[Eu(NO$_3$)$_3$·5H$_2$O, 99.99%] were utilized as initial and dopant precursors, respectively. In all of the samples, the undoped and Eu^{3+}-doped precursors were prepared by dissolving an inappropriate amount of pure methanol (99.8 vol%). Optimum Eu^{3+} ratio was determined as 1.5 wt% to obtain strongest emission intensity [6, 17]. Glacial acetic acid (≥ 99.7 vol%) was added to the solution as a chelating agent for adjusting pH level, increasing the solubility of Ce and Eu in methanol, and obtaining a homogenous solution. All solutions were stirred under magnetic stirring for 30 min until attaining transparent solutions. The same solutions were used in both sol–gel and flame spray production. For the sol–gel production, sol to gel transformation was obtained after keeping at 80 °C for 30 min. Then, the drying process was carried out at 280 °C for 2 h. Subsequently, dried powder was annealed at 600 °C for 2 h to attain crystalline structures. For then FSP synthesis, flame spray pyrolysis equipment (Tethis Nps10) was used to obtain nanoparticles following the same procedure of our previous study [14] with by feeding these solutions into the precursor syringe. All chemicals and solvents were purchased from Sigma Aldrich and used without any further purification.

Determination of phase and crystal structures of the undoped and Eu^{3+}-doped powders was carried out by an X-ray diffractometer (XRD, Thermo Scientific ARL) which operates with 45 kV voltage and 44 mA current settings, and uses Cu-Kα radiation (1.5405 Å). XRD data were recorded with a scanning speed of 2º/min in the range of 20º ≤ 2θ ≤ 80º. Rietveld refinement by Maud (V2.71) program was used for obtaining structural parameters. X-Ray photoelectron spectroscopy (XPS, Thermo Scientific K-Alpha) with a monochromatic Al-Kα (1486.7 eV) X-ray source and a beam size of 400 nm diameter was carried out to determine elemental composition and surface chemistry for all samples. The instrument was calibrated in accordance with gold; 4f$_{7/2}$. The pressure of the system was kept at below 5×10^{-10} mbar for the period of data acquisition. The XPS data of the survey scan was performed from − 10 to 1350 eV with a scanning speed of 1 eV applying pass energy of 150 eV. Whole samples were scanned 20 times from a single point. XPS spectra showed up binding energies of Ce3d, O1s, C1s, and Eu3d. For high-resolution elemental spectra, the pass energy and the scan numbers were 30 eV and 15, respectively. Binding energies and deconvoluted spectra were achieved using the curve fitting application (Thermo Advantage V5.65). Microstructure images of particles were captured at different magnification by scanning electron microscope (SEM, Zeiss Sigma 300 VP) with 20 kV accelerating voltage.

Steady-state PL emission spectra were measured using Edinburgh instruments FLSP 920 fluorescence spectrometer. Fluorescence decay time measurements were performed by single photon counting technique (TCSPC) of the FLSP 920.

The instrument was equipped with a standard 15 W xenon lamp and a micro-second flash lamp for steady-state and lifetime measurements, respectively. The decay time parameters were recovered by iterative convolution with a weighted, nonlinear least squares method using the measured IRF and emission decay data. The reduced chi square values were less than 1.2 and the residuals were symmetrically distributed around the zero axes. Finally, the optical band gap were calculated from the excitation spectra of the samples.

3 Results and discussion

3.1 Phase analysis

XRD patterns of undoped and Eu^{3+}-doped CeO_2 particles produced by different processes are shown in Fig. 1. The XRD patterns show peaks of CeO_2, corresponding to the (111), (200), (220), (311), (222), (400), (331), and (420) crystallographic plane cubic fluorite structure [space group Fm3m (225)] according to the standard data JCPDS Card No. 34-0394. The positions of the peaks are in an agreement with the literature. [19–23]. A slight shift observed in the peak (111) is thought to be due to the dopant incorporated structure and low grain size. The XRD pattern of high purity
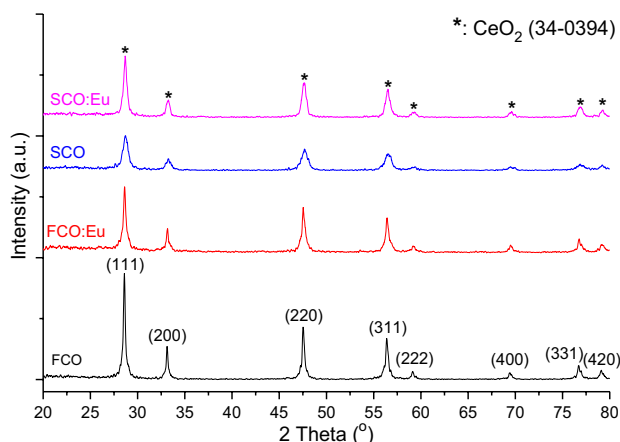

Fig. 1 XRD patterns of nanoparticles

nanoparticles was not observed in any other phase. As the particles become nano-sized, the patterns broaden [21].

The structural and lattice parameters of the nanoparticles were analyzed with the Rietveld refinement using the Maud 2.79 V software and listed in Table 1. The crystallite sizes were calculated from the broadening of the highest peak (111) of the sample using Debye–Scherrer's formula; $D = k\lambda/\beta\cos\theta$, where D is the crystallite size (nm), $k = 0.94$, $\lambda_{Cu} = 0.15406$ nm, β is the full-width at half-maximum of the peak in radians corrected from instrumental broadening, and, θ is the peak angle [18, 24]. The values of lattice parameters are 5.410, 5.406, 5.395, and 5.401 Å for FCO, FCO:Eu, SCO and SCO:Eu samples, respectively. The calculated cell parameter (a) is a little smaller than that of bulk CeO_2 (5.411 Å). This may be due to the lattice constriction effect resulting from Eu^{3+} ions and oxygen vacancies. The crystallite sizes of undoped and Eu^{3+}-doped CeO_2 particles were found to be 22.4, 33.3, 43.1 and 46.2 nm for FCO, FCO:Eu, SCO and SCO:Eu, respectively. The enhancement in the crystallite size of the Eu^{3+} doped particles can be attributed to the radius of Eu^{3+} ($r = 0.1066$ nm) which is larger than the radius of Ce^{4+} ($r = 0.097$ nm), and consequently, the Eu^{3+} occupies more site then the Ce^{4+} [25]. Although the crystal size parameters of the undoped and doped forms were different, the differentiation of the synthesis method did not affect the crystal formation. In addition, the cause of a very small change in the lattice parameters is due to incorporated of the Eu^{3+} ions that entered as interstitial and substitutional atoms in the CeO_2 lattice structure.

3.2 Elemental analysis (XPS)

XPS measurements were carried out to determine the surface chemical composition of all samples whose existing elements, binding energies (BE), and weight concentration (wt%) are summarized in Table 2. The binding energy peaks around 883 eV for the Ce3d, 531 eV for the O1s, and 285 eV for the C1s were in evidence for both undoped and Eu^{3+}-doped CeO_2 which were shown in Fig. 2a. The observed C1s peaks for all samples are expected to be derived from the fortuitous hydro-carbon from the external contaminants or XPS instrument itself which are in

Table 1 Detailed crystallographic parameters of FCO, FCO:Eu, SCO and SCO:Eu nanoparticles

Samples	2θ of crystal plane (111)	Lattice parameters (Å) a = b = c	Unit cell volume (Å)³	Average crystallite Size (nm)	d-spacing (Å)
CeO_2 (JCPDS 34-0394)	28.55	5.411	158.46	–	3.123
FCO	28.60	5.410	158.34	22.4	3.123
FCO:Eu	28.62	5.406	157.99	33.3	3.121
SCO	28.69	5.395	157.03	43.1	3.124
SCO:Eu	28.68	5.401	157.55	46.2	3.121

Table 2 Binding energy (BE) and atomic weight % values according to XPS survey analysis of all samples

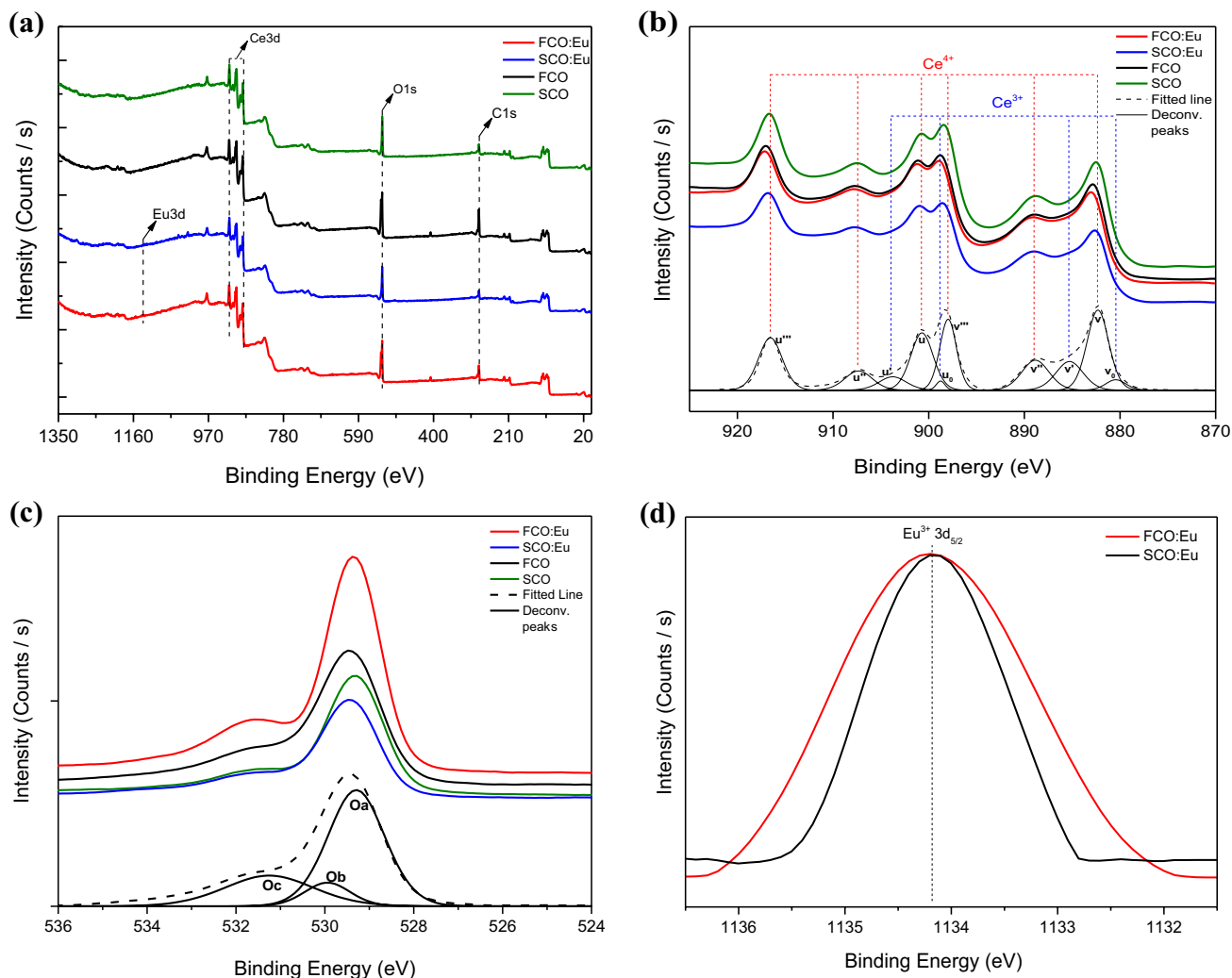| Name	FCO		FCO:Eu		SCO		SCO:Eu	
	Peak BE	Weight %	Peak BE	Weight %	Peak BE	Weight %	Peak BE	Weight %
Ce3d	883.41	47.91	883.45	54.08	883.12	60.72	883.28	60.46
O1s	531.54	30.03	531.12	29.49	530.03	24.21	530.14	24.56
C1s	285.15	22.06	285.16	14.86	285.14	15.07	285.10	13.47
Eu3d			1134.21	1.57			1134.16	1.51

Fig. 2 Represents the **a** XPS survey scans of undoped and Eu^{3+} doped CeO_2 produced by both sol–gel and flame spray pyrolysis methods, **b** Ce3d and **c** O1s core level spectra for FCO, FCO:Eu, SCO, and SCO:Eu fitted line and deconvoluted peaks, **d** $Eu3d_{5/2}$ states of doped samples

agreement with the peak positions and values that reported in the literature [26]. Table 2 shows the binding energy of the Ce3d, O1s, C1s, and Eu3d and atomic weight % for all samples titled FCO, FCO:Eu, SCO, and SCO:Eu.

Figure 2b. shows the core level spectra of Ce3d for the FCO, FCO:Eu, SCO, and SCO:Eu, respectively. The deconvoluted fitted lines are related to the valance levels of the Ce which are labeled as u_0, u', u'', u''' and v_0, v', v'', v'''.

While the u_0, u', and v_0, v', are characteristics peaks of the Ce^{3+} ions the u'', u''' and v'', v''' are belonged to the Ce^{4+} ions [27–34] which means CeO_2 has mixed valance states. Because of the presence of both 3+ and 4+ oxidation states besides multiple d-splitting together, the deconvoluted spectra is relatively complex.

The group 'u' is related to $3d_{3/2}$ while group 'v' is related to $3d_{5/2}$ states and main peaks of these states are shown

with 'u‴' and 'v‴' at 916.58 ± 0.7 eV and 898.6 ± 0.7 eV, respectively. These peaks correspond to $3d^{10}4f^0$ state of the Ce^{4+} ions [27, 28]. The 'u″ (907.38 eV), u (900.78 eV)' and 'v″ (888.78 eV), v (882.38 eV)' are two satellite peaks which located lower binding energy positions for each main peaks (u‴ and v‴). On the other hand, the u′ (903.92 eV) and v′ (885.34 eV) are belong to the $3d^{10}4f^1$ configuration of the Ce^{3+} ions [27, 28]. Similarly the Fig. 2c shows the core level spectra of O1s for the FCO, FCO:Eu, SCO, and SCO:Eu. The fitted line and deconvoluted graph which are labeled as Oa, Ob, and Oc, give peaks at 529.28 ± 0.2 eV, 529.94 ± 0.2 eV and 531.30 ± 0.2 eV, respectively. The Oa and Ob are related to the oxygen bonds to Ce^{4+} and Ce^{3+} [28, 31, 35] while the Oc is associated with hydroxyls and/or H_2O molecules bond to Ce^{3+} [28, 31, 36], respectively. The Oa peak with the lowest binding energy of O1s core level spectra is related to O^{2-} ions surrounded by the Ce^{4+} ions at Ce–O bond in CeO_2 and the Ob peak can be attributed to the O^{2-} ions at Ce–O bond which include the Ce as 3+ valance state. The Oc peaks belong to the O^{2-} ions which are proper to the Eu^{3+}–O^{2-} configuration [28, 37]. And, while the Oa is related to the lattice oxygen, the Oc belongs to the oxygen vacancies [30]. The characteristic peaks of $Eu3d_{5/2}$

(1134.19 eV) which is shown in Fig. 2d indicated that the Eu is in the trivalent state at Eu doped samples [28, 33].

3.3 Particle morphology (SEM)

The SEM images of undoped CeO_2 and Eu^{3+} doped CeO_2 powders produced through SG and FSP are depicted in Fig. 3. Eu^{3+} doped CeO_2 powders fabricated by SG method were found to be agglomerated within a wide size range between Fig. 3a, b. However, the FSP based powders exhibited agglomerates in nanoscale (size) that are formed by spherical particles in a uniform distribution. As can be seen from the images in SG based powders complex geometries with sharp edges were observed. The SEM images of both SG and FSP based powders are in a good agreement with the literature [29, 38] for, in which they observed similar behavior.

3.4 Photoluminescence properties

As far as it is known, the luminescence properties of the CeO_2 arise from its cubic fluorite-type crystal structure and the Ce^{4+} is not possessed of the 4f electrons. However,
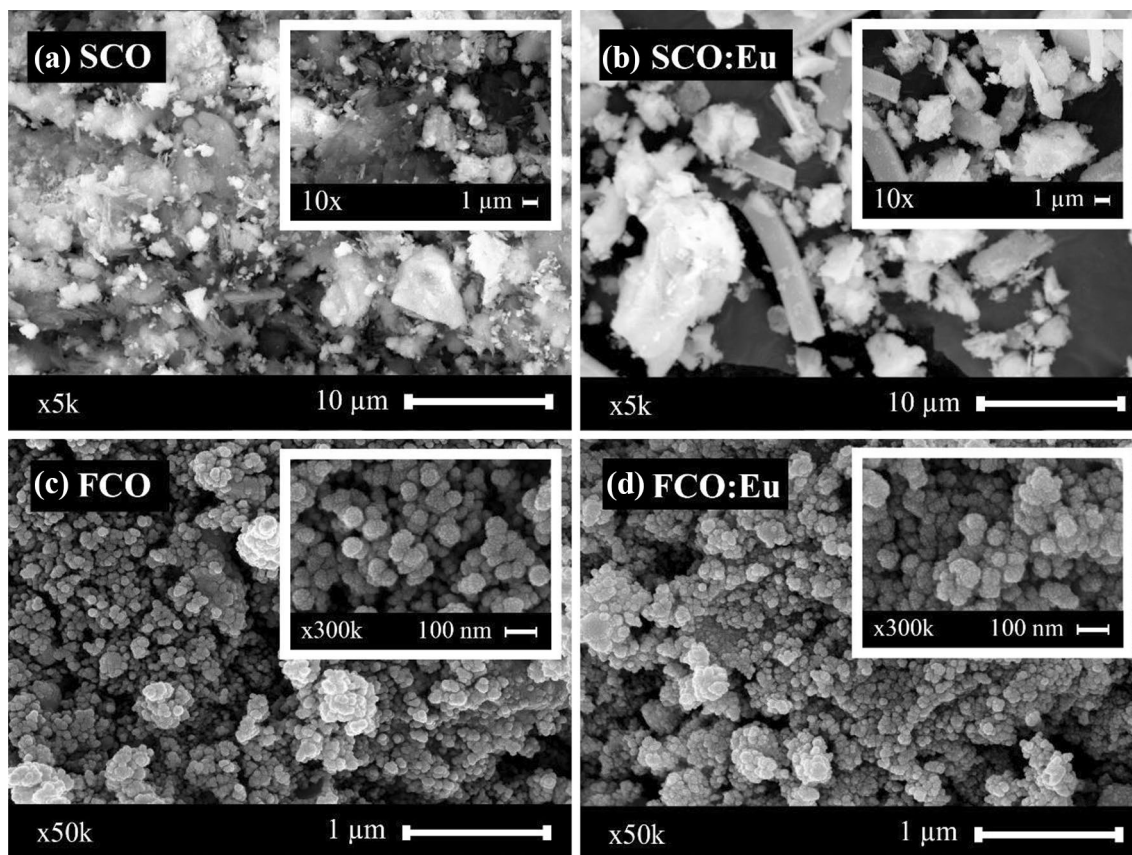

Fig. 3 The SEM micrographs of FCO, FCO:Eu, SCO and SCO:Eu nanoparticles

the Eu^{3+} ion-doped ceria become a remarkable luminescent material. Herein, the room temperature PL analysis of undoped and the Eu^{3+}-doped CeO$_2$ nano-powders, which is fabricated, by the SG and FSP methods has been carried out.

Figure 4 shows excitation-emission spectrum of CeO$_2$ and CeO$_2$:Eu^{3+} that synthesized by both of the FSP and the SG. When we compare the CeO$_2$:Eu^{3+} and the CeO$_2$, the emission maxima of the fabricated nano-powders have significant variations in consequence of the dopant ion.

When both Eu^{3+}-doped and undoped CeO$_2$ material excited at approximately 355 nm, we observed the emission peak maximum at 536 nm for undoped form, behind this there is a significant change for Eu^{3+}-doped CeO$_2$ which resulted with 12–14 nm red-shifted in emission maxima.

When Eu^{3+} is doped to the ceria, the transitions between 4f levels depends on as a cumulative effect of the magnetic and electrical dipole interactions cause the observation of the emission peaks between 590 and 660 nm [28, 39]. In order to achieve an effective energy transfer, optimal spectral overlap of CeO$_2$ and Eu^{3+} is important. The strong and intense red light in the emission spectrum shows that the energy levels of Eu^{3+} are suitable to receive energy from Ce^{4+}. Although the Eu-doped ceria has sharp peaks observed at around 590, 610, 630 and 650 nm, which is the specific 4–4f, transitions for Eu^{3+} in for both synthesis, the pure ceria does not show any peaks stated emission band. The emission spectrum showed the characteristic peaks of the Eu^{3+} that related to the various transitions of $^5D_0$–^7F_J (J = 0, 1, 2, etc.) which shows off more information about the environment and symmetry of the Eu^{3+} ions [40, 41]. The Eu^{3+}-doped CeO$_2$ nanocrystals showed remarkable enhancement at a wavelength between 590 and 655 nm in the emission spectrum, because of the increased oxygen vacancies, the charge compensation effect and the improvement of crystallinity.
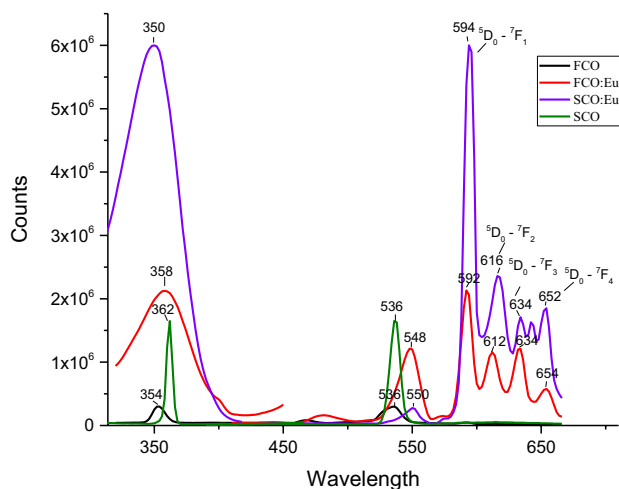

Fig. 4 Excitation and emission spectra of CeO$_2$ and CeO$_2$:Eu^{3+} for both FSP and SG

The crystallite size of Eu^{3+}-doped CeO$_2$ synthesized by the SG method have bigger when compared with the obtained Eu^{3+}-doped ceria nanocrystals by the FSP. Therefore, the increment with the crystallite size of ceria caused the improvement of the emission intensities of the plural peaks in the red emission band. It can be attributed to the enhancement of crystallinity as well as charge compensation.

The specific emission peak depends on the symmetry of Eu-substituted CeO$_2$ crystal sites. For CeO$_2$:Eu, Eu^{3+} ions replaced in highly symmetric Ce^{4+} sites. In Fig. 4, for both FSP and SG synthesis techniques, the dominant red emission band of Eu^{3+}, which is situated at around 590 nm, is due to magnetic dipole transition of $^5D_0 \rightarrow ^7F_1$ of inside Eu^{3+} ion with 4f configurations. On the contrary, the electric dipole transitions, $^5D_0 \rightarrow ^7F_2$ (~614 nm), $^5D_0 \rightarrow ^7F_3$ (~634 nm) and $^5D_0 \rightarrow ^7F_4$ (~653 nm) transitions are allowed when Eu^{3+} ions are in the sites without the inversion symmetry. These situations show that Eu^{3+} ions are actually doped into the CeO$_2$ crystal lattice by both the FSP and the SG synthesis methods.

According to the excitation/absorption peak electrons absorb the energy at a certain specific wavelength and so energy absorbing electrons are going to excited state from ground state. This means that related material is having a band gap that can be determined by absorption or excitation wavelength. The optical band gap of both undoped and Eu^{3+}-doped CeO$_2$ nanoparticles synthesized by FSP and SG was found using the formula [6].

$$E_g(eV) = 1240/\lambda_g \quad (1)$$

in which 'λ_g' is the maximum wavelength of the excitation spectra (See Eq. 1). The optical band gap values of for both undoped and Eu^{3+}-doped CeO$_2$ material excited at 354 nm, 358 nm for FSP and 362 nm, 350 nm for SG methods are found 3.50, 3.46, 3.42, 3.54, respectively. Our results are in good agreement with the study of literature [17, 42–44], in which they measured the approximately the same optical band gap values for un-doped and doped CeO$_2$ nanoparticles.

Figure 5 shows decay curves of the CeO$_2$ and CeO$_2$:Eu^{3+} fabricated by both FSP and SG methods respectively. The synthesized nanoscale powders were excited with a microsecond flash lamb at 536 nm, 550 nm, 536 nm, and 548 nm, respectively. All of the composites exhibited three-exponential decays. Table 3 reveals the results of the decay time measurements of the free form and the Eu^{3+} doped ceria nano-powders along with the standard deviation and percentage distribution. The average decay times of 88.20 and 102.06 μs have been calculated for the sol–gel synthesized SCO and SCO:Eu^{3+}, respectively. Similarly, the flame spray synthesized forms exhibited average decay times of 53.11 and 92.00 μs for the Eu^{3+}-free and Eu^{3+}-doped forms. In both cases, the presence of the Eu^{3+} enhanced the decay time 16 and 73% respectively which was evidenced in our

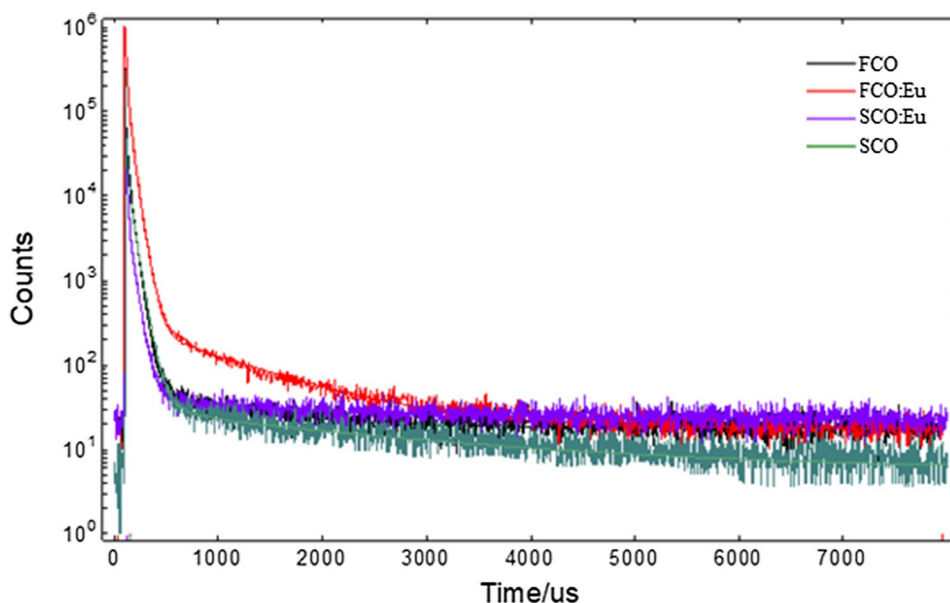**Fig. 5** Decay curves of CeO_2 and CeO_2:Eu^{3+} for both FSP and SG

Table 3 Decay time measurements of CeO_2 and CeO_2:Eu^{3+} for both FSP and SG

Sample	λ^{ex}, λ^{em} (nm)	χ^2		Decay time (µs)	Std. dev. (µs)	Rel. (%)
SCO	362, 536	1.197	τ_1	10.6884	0.13248	43.04
			τ_2	53.1476	0.39911	52.97
			τ_3	1389.6815	107.76449	3.99
			τ_{avr}	88.20		
SCO:Eu	350, 550	1.130	τ_1	6.5478	0.12116	57.97
			τ_2	38.8073	3.02599	14.41
			τ_3	335.535	14.97439	27.62
			τ_{avr}	102.06		
FCO	354, 536	1.271	τ_1	13.2906	0.17128	31.60
			τ_2	47.6824	0.22243	66.41
			τ_3	862.2902	35.71045	2.00
			τ_{avr}	53.11		
FCO:Eu	358, 548	1.362	τ_1	28.3657	0.66566	36.26
			τ_2	57.0564	0.67120	58.59
			τ_3	934.2767	12.99072	5.15
			τ_{avr}	92.00		

previous work [45]. Decay times of the Eu^{3+}-free sol–gel synthesized particles were longer with respect to the flame spray-synthesized ones. The observation of the three exponential decay times can be attributed to the structural properties of the host matrix (CeO_2) and the formation of three different microenvironments for the Eu^{3+} dopant.

4 Conclusion

The undoped and Eu^{3+}-doped CeO_2 particles were successfully synthesized by flame spray pyrolysis and sol–gel methods. The cubic fluorite structure and the crystallite size between 22 and 46 nm of the obtained powders were determined using XRD. The morphology of the particles synthesized by the sol–gel method was observed to be in a wide range of sizes and shape, while the particles produced by the FSP method were determined to be below 100 nm and spherical shape. XPS analysis showed that Eu element was successfully incorporated into the structure. In this study, in comparison with the two different production techniques, luminescence results played an important role in revealing the presence of the Eu^{3+} in the lattice. Additionally, the Eu-doped particles exhibited longer decay time than the undoped particles and particle size did not significantly affect luminescence properties within the frame of the study.

References

1. M. Fernández-García, J.A. Rodriguez, Encycl. Inorg. Bioinorg. Chem. (2011). https://doi.org/10.1002/9781119951438.eibc0331
2. F. Charbgoo, M. Bin Ahmad, M. Darroudi, Int. J. Nanomed. **12**, 1401 (2017)
3. G. Wang, Q. Mu, T. Chen, Y. Wang, J. Alloys Compd. **493**, 202 (2010)
4. S. Schmitt-Rink, C.M. Varma, A.F.J. Levi, Phys. Rev. Lett. **66**, 2782 (1991)
5. L. Li, H.K. Yang, B.K. Moon, Z. Fu, C. Guo, J.H. Jeong, S.S. Yi, K. Jang, H.S. Lee, J. Phys. Chem. C **113**, 610 (2008)
6. G. Vimal, K.P. Mani, P.R. Biju, C. Joseph, N.V. Unnikrishnan, M.A. Ittyachen, Appl. Nanosci. **5**, 837 (2015)
7. Q. Yuan, H.-H. Duan, L.-L. Li, L.-D. Sun, Y.-W. Zhang, C.-H. Yan, J. Colloid Interface Sci. **335**, 151 (2009)
8. X.-D. Wang, X.-H. Liu, S.-J. Chen, M. Li, M. Liu, Spectrosc. Spectr. Anal. **27**, 2182 (2007)
9. T. Masui, K. Fujiwara, K. Machida, G. Adachi, T. Sakata, H. Mori, Chem. Mater. **9**, 2197 (1997)
10. I. Yamaguchi, M. Watanabe, T. Shinagawa, M. Chigane, M. Inaba, A. Tasaka, M. Izaki, ACS Appl. Mater. Interfaces, **1**, 1070 (2009)
11. I. Yamaguchi, M. Watanabe, T. Shinagawa, M. Chigane, M. Inaba, A. Tasaka, M. Izaki, ACS Appl. Mater. Interfaces **1**, 1070 (2009)
12. M. Dubau, J. Lavková, I. Khalakhan, S. Haviar, V. Potin, V. Matolín, I. Matolínová, ACS Appl. Mater. Interfaces **6**, 1213 (2014)
13. T. Masui, H. Hirai, N. Imanaka, G. Adachi, T. Sakata, H. Mori, J. Mater. Sci. Lett. **21**, 489 (2002)
14. L. Mädler, H.K. Kammler, R. Mueller, S.E. Pratsinis, J. Aerosol Sci. **33**, 369 (2002)
15. T. Sahm, L. Mädler, A. Gurlo, N. Barsan, S.E. Pratsinis, U. Weimar, Sensor Actuat B-Chem. **98**, 148 (2004)
16. H.Q. Zhou, M. Wang, X. Jiang, G.J. Liu, Q. Gu, S.T. Liu, Adv. Mater. Res. **79**, 597 (2009)
17. M. Oikawa, S. Fujihara, J. Eur. Ceram. Soc. **25**, 2921 (2005)
18. S. Yildirim, E.C. Karsu Asal, K. Ertekin, E. Celik, J. Lumin. **187**, 304 (2017)
19. E. Longo, M. Ramirez, L.S.R. Rocha, A.Z. Simões, J. Cortés, R. Deus, M.A. Ponce, J. Andres, Mater. Res. Bull. **70**, 416 (2015)
20. Z.-L. Wang, G.-R. Li, Y.-N. Ou, Z.-P. Feng, D.-L. Qu, Y.-X. Tong, J. Phys. Chem. C **115**, 351 (2011)
21. A.A. Ansari, J. Semicond. **31**, 053001 (2010)
22. I.V. Zagaynov, S.V. Kutsev, Appl. Nanosci. **4**, 339 (2014)
23. S. Fujihara, M. Oikawa, J. Appl. Phys. **95**, 8002 (2004)
24. Mİ. Katı, O. Yılmaz, S. Gültekin, E. Çelik, S. Yıldırım, İ.Ç. Keskin, J. Lumin. **206**, 59 (2018)
25. L. Li, H.K. Yang, B.K. Moon, Z. Fu, C. Guo, J.H. Jeong, S.S. Yi, K. Jang, H.S. Lee, J. Phys. Chem. C **113**, 610 (2009)
26. J.F. Moulder, in *Handbook of X-ray Photoelectron Spectroscopy: A Reference Book of Standard Spectra for Identification and Interpretation of XPS Data*, ed. by J. Chastain, R.C. King Jr (Physical Electronics, Eden Prairie, MN, 1995)
27. K. Kuntaiah, P. Sudarsanam, B.M. Reddy, A. Vinu, RSC Adv. **3**, 7953 (2013)
28. A. Kumar, S. Babu, A.S. Karakoti, A. Schulte, S. Seal, Langmuir **25**, 10998 (2009)
29. G.B. Della Mea, L.P. Matte, A.S. Thill, F.O. Lobato, E.V. Benvenutti, L.T. Arenas, A. Jürgensen, R. Hergenröder, F. Poletto, F. Bernardi, Appl. Surf. Sci. **422**, 1102 (2017)
30. J.M. López, A.L. Gilbank, T. García, B. Solsona, S. Agouram, L. Torrente-Murciano, Appl. Catal. B **174–175**, 403 (2015)
31. C. Barth, C. Laffon, R. Olbrich, A. Ranguis, P. Parent, M. Reichling, Sci. Rep. **6**, 2 (2016)
32. T. Naganuma, E. Traversa, Biomaterials **35**, 4441 (2014)
33. S. Babu, A. Schulte, S. Seal, Appl. Phys. Lett. **92**, 1 (2008)
34. S. Deshpande, S. Patil, S.V. Kuchibhatla, S. Seal, Appl. Phys. Lett. **87**, 1 (2005)
35. T. Hasegawa, S.M.F. Shahed, Y. Sainoo, A. Beniya, N. Isomura, Y. Watanabe, T. Komeda, J. Chem. Phys. **140**, 044711 (2014)
36. M.A. Henderson, C.L. Perkins, M.H. Engelhard, S. Thevuthasan, C.H.F. Peden, Surf. Sci. **526**, 1 (2003)
37. C.D. Wagner, D.A. Zatko, R.H. Raymond, Anal. Chem. **52**, 1445 (1980)
38. M. Melchionna, P. Fornasiero, Mater. Today **17**, 349 (2014)
39. H. Guo, Y. Qiao, Appl. Surf. Sci. **254**, 1961 (2008)
40. K.Y. Jung, J.C. Lee, D.S. Kim, B.K. Choi, W.J. Kang, J. Lumin. **192**, 1313 (2017)
41. M. Maheshwary, S. Singh, B.P. Singh, P. Singh, R.A. Singh, S.B. Rai, S. Singh, V.K. Sonu, P.V. Ramakrishna, A. Bahadur, RSC Adv. **5**, 55977 (2015)
42. Z.C. Orel, B. Orel, Phys. Status Solidi **186**, K33 (1994)
43. S. Demirci, B. Öztürk, S. Yildirim, F. Bakal, M. Erol, O. Sancakoğlu, R. Yigit, E. Celik, T. Batar, Mater. Sci. Semicond. Process. **34**, 154 (2015)
44. A.V. Emeline, G.N. Kuzmin, D. Purevdorj, V.K. Ryabchuk, N. Serpone, J. Phys. Chem. B **104**, 2989 (2000)
45. S. Yildirim, S. Demirci, K. Ertekin, E. Celik, Z.A. Alicikus, J. Adv. Ceram. **6**, 33 (2017)